Northumbria Research Link

Northumbria
University
NEWCASTLE

Multiphysics Structured Eddy Current and Thermography Defects Diagnostics System in Moving Mode

Abstract - Eddy current testing (ET) and eddy current thermography (ECT) are both important non-destructive testing (NDT) methods that have been widely used in the field of conductive materials evaluation. Conventional ECT systems have often employed to test static specimens eventhough they are inefficient when the specimen is large. In addition, the requirement of high-power excitation sources tends to result in bulky detection systems. To mitigate these problems, a moving detection mode of multiphysics structured ET and ECT is proposed in which a novel L-shape ferrite magnetic yoke circumambulated with array coils is designed. The theoretical derivation model of the proposed method is developed which is shown to improve the detection efficiency without compromising the excitation current by ECT. The specimens can be speedily evaluated by scanning at a speed of 50-250 mm/s while reducing the power of the excitation current due to the supplement of ET. The unique design of the excitation-receiving structure has also enhanced the detectability of omnidirectional cracks. Moreover, it does not block the normal direction visual capture of the specimens. Both numerical simulations and experimental studies on different defects have been carried out and the obtained results have shown the reliability and detection efficiency of the proposed system.

Index terms - Non-destructive testing (NDT), eddy current testing (ET), eddy current thermography (ECT), moving mode

I. INTRODUCTION

With the rapid development of manufacturing industry, the types and quantities of industrial products have proliferated. It is important to efficiently detect the infrastructures while ensuring its reliability and safety [1]-[3]. Non-destructive testing (NDT) is commonly used for such analysis without changing the inherent characteristics of a component [4]-[6].

There are extensive NDT methods for near-surface defect detection such as Magnetic Particle Testing (MT), Penetrant Testing (PT), Ultrasonic Testing (UT), Radiographic Testing (RT), Eddy Current Testing (ET) and Eddy Current Thermography (ECT). MT is good at detecting the discontinuities in the surface and subsurface of ferromagnetic materials with small dimensions and extremely narrow gaps. Unfortunately, it requires high surface smoothness of the tested parts and rich experience of the inspectors. Simultaneously, the detection area of MT is small and the speed is slow [7]. PT is not limited by the chemical composition, structure, and shape of the workpieces, and it is especially sensitive to opening surface cracks. However, the inspection is complicated and it produces pollution [8]. UT can detect deeper flaws because of its strong penetrability whereas it is hard to inspect workpieces with complex shapes and also requires couplant [9][10]. RT provides accurate, intuitive images whereas the shortcomings are also obvious, such as high cost, slow speed and harmful to human beings with the accident [11].

Both ET and ECT play huge roles in the field of conductive materials evaluation due to their reliability and feasibility. ET is one of the most efficient NDT methods which has been widely used for crack detection at relatively high speeds without any direct physical contact between the coil probes and the inspected pieces. Nevertheless, it remains difficult to quantify the defects due to the limited impedance or voltage signals from detection coils [12][13]. As another homologous technique, ECT has received increasing attention from researchers since its inception. The main advantage of ECT is that it can quickly evaluate a fixed area with high spatial resolution and sensitivity within a short excitation period (typically one hundred to several hundred ms) [14]-[16]. In addition, ECT has made some progress in the detection of geometrically heterogeneous specimens [17][18]. Regrettably, ECT systems are mainly used for static specimens testing where it is inefficient and less sensitivity for defects diagnostics across the whole aspect of the large samples as well as the limitation requirement of the high-power excitation source [19][20].

To mitigate these problems, several researches have been carried out. Macecek proposed an advanced eddy current array to demonstrate the direction and empirical sizing of cracks and corrosion spots in low conductivity aluminum sheets [21]. Sun *et al*. designed a flexible arrayed eddy current sensor to improve the sensibility of hollow axle inner surface defects detection [22]. Endo *et al*. applied an ET system with multi-coil type probes to size up cracks fabricated on austenite stainless plates [23]. He *et al*. presented a moving mode of eddy current thermography to investigate the artificial defect feature extraction methods which are suitable in the moving mode [24]. He *et al*. found a method for suppression of the effect of uneven surface emissivity of material in the moving mode of eddy current thermography [25]. Gao *et al*. reported a ferrite yoke based on ECPT to enhance the detectability of multiple cracks [26]. Li *et al*. illustrated a Helmholtz-coil based ECPT configuration for the state detection and characterization of bond wire lift-off in IGBT modules [27]. Liu *et al*. proposed an L-shaped sensor to diagnose natural cracks in a static system [28]. Goldammer *et al*. showed how NDT can be automated using as an example of industrial applications at the Siemens sector Energy [29]. Streza *et al*. used an active thermography approach to improve the testing efficiency of thermoelectric materials [30]. However, there exists limited researches concentrated on the physics-based coupling of both thermal and electromagnetic fields to jointly build a diagnosis system.

In this paper, a moving mode detection of multiphysics structured ET and ECT in which a novel L-shape ferrite magnetic yoke surround with array coils is proposed. The model is based on the multiphysics coupling mechanism that the induced eddy current generates thermal and electro-magnetic fields synchronously. In this model, the advantages of ET and ECT complemented each other. On the one hand, quantifying and imaging the defects using ET remains difficult due to the limited impedance or

voltage signals from the detection coils. Although there are research studies where ET systems have been applied with array coil probes, poor imaging caused by low resolution still remains a problem. ECT plays an important role that it leverages its visually capability to detect the defects with high spatial resolution, and the dimensions (length and width) of the defects can be measured in the thermal images. At this juncture, it should be noted that without the contributions of ECT, the shape of the defects cannot be directly measured. On the other hand, ECT is easily be influenced by the impact of the surface condition such as variation of emissivity. In this respect, ET detection plays an important role to distinguish the abnormal signal between defects and surface conditions. In conclusion, with the aid of a conveyor belt, specimens can be evaluated fast by scanning at the speed of 50-250 mm/s as well as reducing the power range of the excitation current due to the supplement of ET. In addition, the high spatial resolution and sensitivity of the structured ET linked to ECT can be used to quantify the defects more accurately.

The rest of this paper is organized as follows: Section 2 presents the basic theory of the new configuration of ET and ECT. Section 3 describes the implementation of the system as well as the simulation and experiment studies along the results. Section 4 concludes the proposed work and summarizes the future direction of the work.

II. METHODOLOGY

A. Configuration of the coupling structured system

The schematic diagram of the coupling structured system is shown in Fig. 1 (a). The self-designed digital inductive device based on an FPGA controller is implemented to generate high-frequency alternating currents. It can drive the L-shape ferrite magnetic core and induce the eddy current as well as produce the resistive heat in the conductive materials. The diagram of the excitation-receiving structure is shown in Fig. 1 (b), array coils are placed around the yoke by a 3D printing holder which is perfectly fit to the shape of the yoke, the red dotted area represents the region of interest (ROI) of the IR camera. It should be noted that the ROI is not blocked due to the special design of the core. An object will continuously absorb or emit infrared radiation due to the constant motion of charged particles when the temperature of the object is above the absolute zero. According to Lambert's law of cosines, the radiant intensity I_θ is the radiant power that is emitted from a point source of a radiating object into a solid angle element in the given direction [28]:

$$I_\theta = I_0 \cos\theta \qquad (1)$$

where I_0 denotes radiation intensity in the normal direction of the surface, θ denotes the angle between the observed direction and surface normal. It indicates that the radiation intensity is the strongest in the normal direction of the surface. Therefore, the viewing angle of the IR camera should be selected to the normal direction of the surface and it can be satisfied by using of the proposed L-shape yoke. The angular dependence of radiant intensity is schematically depicted in Fig. 1 (c).

The purpose of the placement of coil1 is to detect the horizontal defects (perpendicular to the induced eddy current) that are insensitive to coil2-coil4. For vertical defects (parallel to the induced eddy current), the sequence information can be captured by coil2 and coil4 arrays as they are more sensitive to it while the magnetic flux near the end of the yoke poles is dense in the z-direction and the changes of the voltage in coil2 and coil4 are more pronounced. In terms of coil3, it is an important position to capture both electromagnetic and thermal signals simultaneously. All coils are applied to capture both spatial and time sequences information in order to accurately locate the defects. A speed-controlled conveyor belt is employed other than the excitation, thermal imaging, and data acquisition systems in this moving mode of the multiphysics structured pattern.

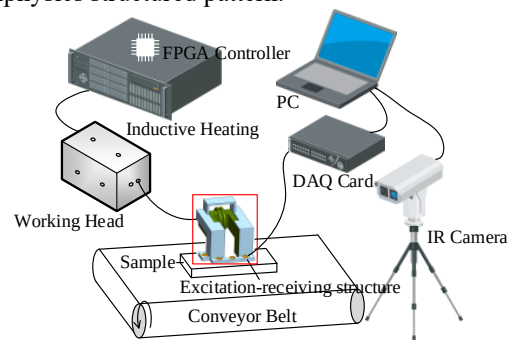

Fig. 1 (a) Schematic diagram of the coupling structured system.

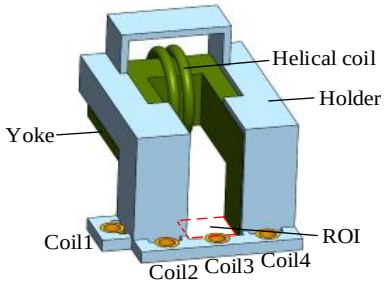

Fig.1 (b) Diagram of the excitation-receiving structure.

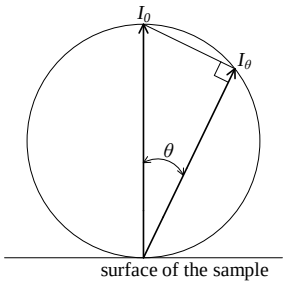

Fig.1 (c) The radiant intensity depends on the direction of emission.

When the FPGA controller provides a switch drive signal, high-frequency alternating current flows through the helical coil which is wound round the yoke and its turns number is 2, the radius and wire diameter are 12.5 mm and 4 mm, respectively. It generates alternating magnetic field and the ferrite magnetic core guides the magnetic flux through its shape and the flux is transmitted to the specimens by the two poles of the core. In that way, strong eddy currents are generated on the near-surface of the metal plate and can be acquired by both detection coils and an IR camera. With the movement of the conveyor belt, the carried specimen will be swept at a certain speed so that the array coils can detect the changes in the voltage signals and the IR camera can capture the disturbance of the temperature distribution when there are cracks on the near-surface of the specimens. Thus, two types of signals (i.e. electromagnetic and thermal) are acquired simultaneously with one excitation.

B. Mathematical models of the electromagnetic field

Without considering the speed effect, electromagnetic field differential equation derived from Maxwell's equation can be drawn as:

$$\nabla \times \frac{1}{\mu}(\nabla \times \vec{A}) = \vec{J} - \sigma \frac{\partial \vec{A}}{\partial t} \quad (2)$$

where $\vec{A}$ is the vector potential, $\vec{J}$ is the conduction current density and μ is the magnetic permeability of the medium. The vector potential $\vec{A}$ can be defined as:

$$\vec{B} = \nabla \times \vec{A} \quad (3)$$

where $\vec{B}$ is the magnetic flux density.

Lorentz force can be used to analyze the speed effect problem in the dynamic eddy current detection system. Due to the Lorentz force, when there is relative movement between detecting device and workpiece, the eddy current density equation generated in the specimen is given as:

$$\vec{J_v} = \sigma \vec{v} \times \vec{B} = \sigma \vec{v} \times (\nabla \times \vec{A}) \quad (4)$$

where $\vec{J_v}$ indicates the eddy current density excited in the workpiece, σ is the electrical conductivity and $\vec{v}$ is the relative velocity between detecting device and workpiece.

If Eq. (2) and Eq. (4) are combined to analyze the eddy current detection system under dynamic conditions, the electromagnetic fields differential equation can be transformed as:

$$\nabla \times \frac{1}{\mu}(\nabla \times \vec{A}) = \vec{J} - \sigma \frac{\partial \vec{A}}{\partial t} + \sigma \vec{v} \times (\nabla \times \vec{A}) \quad (5)$$

where $\sigma \frac{\partial \vec{A}}{\partial t}$ denotes the eddy current intensity caused by the change of the magnetic field, $\sigma \vec{v} \times (\nabla \times \vec{A})$ denotes the eddy current intensity caused by the speed effect.

From the differential equation of the electromagnetic fields, the changes of the eddy current intensity are caused by the joint action of magnetic vector potential and speed effect. The eddy current induced by the change of the magnetic vector potential is inversely proportional to its frequency and the velocity-induced eddy current is proportional to the speed as well as magnetic field strength. According to this, it can be inferred that with the speed increases, the velocity-induced eddy current intensity would increase. This principle can be used for crack detection in the moving mode. Nevertheless, if the relative motion speed between the coil and the specimen is slow, this effect is negligle and can therefore be ignored.

In this study, an L-shape core is implemented for magnetism gathering. The magnetic circuit generated by the L-shape core in the space can be summarized into three paths (as shown in Fig. 2). Path I means the magnetic flux leakage produced by the helical coil that does not flow into the core, one of them is expressed as the red dotted loop and assume the average length of them is l_{leak}. Path II includes the flux passing through part of the L-shape core as well as the air between the two poles, one of them is marked as green dotted loop and assume the average length in the core is l_x and in air is l_{air}. Path III includes the flux flow through the entire core and the specimen placed under the ferromagnetic core. Of course, if there are gaps between the core and the sample, the length of the gaps should be taken into consideration. One of the paths is expressed as the purple dotted loop and the total length can be divided into l_{core}, l_{gap}, and l_{sample}. Besides, the flux overflow of the specimen can be ignored.

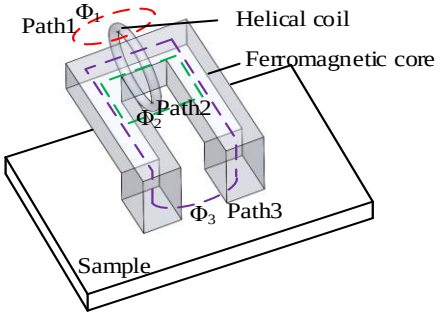

Fig. 2 Magnetic flux paths of the core in space.

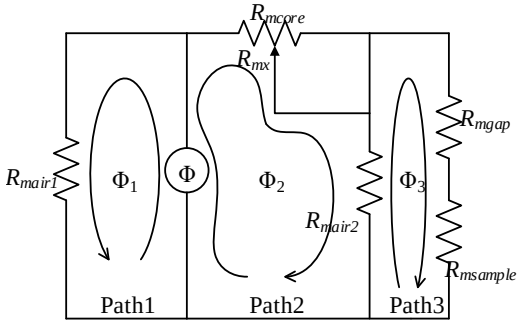

Fig. 3 Equivalent magnetic circuit of the model.

The equivalent magnetic circuit of this model can be simplified as shown in Fig. 3. According to Ohm's law in magnetic, similar to the electric circuit, the magnetic circuit can be derived. The relationship among magnetic flow Φ, magnetomotive force F and magnetic resistance R_m can be written as:

$$F = \Phi R_m = NI \quad (6)$$

where I is the current that generates the magnetic field and N represents the turns of the helical coil.

The magnetic resistances in the path I, II, and III can be denoted as R_{m1}, R_{m2} and R_{m3}. Due to the determination formula of the magnetic resistance, R_{m1}, R_{m2} and R_{m3} can be described as:

$$R_{m1} = R_{mair1} = \frac{l_{leak}}{\mu_0 A_{air1}} \quad (7)$$

$$R_{m2} = R_{mx} + R_{mair2} = \frac{l_x}{\mu_{core} A_{core}} + \frac{l_{air}}{\mu_0 A_{air2}} \quad (8)$$

$$R_{m3} = R_{mcore} + R_{mgap} + R_{msample} = \frac{l_{core}}{\mu_{core} A_{core}} + \frac{l_{gap}}{\mu_0 A_{gap}} + \frac{l_{sample}}{\mu_{sample} A_{sample}} \quad (9)$$

where μ_0, μ_{core}, and μ_{sample} are the magnetic permeability of the air, core, and sample, respectively. A_{air1}, A_{air2}, A_{core}, A_{gap}, and A_{sample} are the valid cross-sectional areas of the air, core, gaps, and sample passed by the magnetic flux. R_{mair1}, R_{mair2}, R_{mcore}, R_{mgap}, and $R_{msample}$ are the magnetic resistances in the air, core, gaps, and sample, respectively. In addition, R_{mx} represents the resistance of the path in part of the core whose length is x.

Thus, from path III, it can be known that the flux is gathered in the area between the two poles of the yoke, it is beneficial to generate stronger eddy currents. Detection coils can be placed around the ends of the core due to the strong electromagnetic induction. In a dynamic system, when a conductive material moves to the underneath of the excitation core, uniform eddy currents generate, and a crack

will obstruct the eddy current flow. This directly leads to the extension of the eddy current path, the induced magnetic field will be reduced and the voltage signal on the coil probe varies. With the departure of the crack, the voltage will revert to the initial value.

C. Mathematical models of the electromagnetic-thermal field

As the tested piece moves, the whole aspect of the sample can be heated by eddy current over time. Thus, the thermal field at each point is a combination of the local induction heating and the surrounding thermal diffusion field. The skin depth of the eddy current is related to the characteristics of the conductive materials and the frequency of the excitation current, it can be described as:

$$\delta = \frac{1}{\sqrt{\pi\sigma\mu f}} \tag{10}$$

where δ is the skin depth and f is the frequency of the excitation current. It is not difficult to find that δ is inversely related to the square-root of the electrical conductivity, magnetic permeability, and excitation frequency.

In the light of Joule's law, heat is generated when eddy currents exist in the specimen. As the heat source, the expression of the eddy current can be shown below:

$$Q = \frac{1}{\sigma}\left|\vec{J}_e\right|^2 + \frac{1}{\sigma}\left|\vec{J}_v\right|^2 \tag{11}$$

where Q is the strength of the generated heat, $\vec{J}_e$ is the eddy current density, $\vec{J}_v$ is the current density generated by the relative motion. The Joule heat which is produced by eddy current can be propagated to other parts of a specimen and this process can be represented as:

$$\rho C\frac{\partial T}{\partial t} = \nabla\cdot(k\nabla T) + Q \tag{12}$$

where ρ, C, k are the density, specific heat, and the heat transfer coefficient of the specimen, respectively. T is the temperature. When speed effect is taken account, the formula should be rewritten as [24]:

$$\rho C\frac{\partial T}{\partial t} + \rho C\vec{v}\cdot\nabla T = \nabla\cdot(k\nabla T) + Q \tag{13}$$

where $\vec{v}$ is the relative velocity of the specimen. It should be noted that while the relative motion speed between the coil and the specimen is slow, the heat generated by $\vec{J}_v$ can be safely neglected.

The eddy currents on the specimen produced by alternating magnetic in this model is shown in Fig. 4. Assuming the moving direction of the specimen is along with the *x*-axis, as a crack moves to position 1, the eddy currents will bypass it and their paths are extended. Since a detection coil is placed above this position, the voltage will be changed dramatically. When the crack moves to position 2, the voltage of the detection coil conduct the variation again due to the same principles. However, the fluctuation at the latter is less obvious because the crack at position 2 obstruct less currents than the former. On the other hand, these two variation construct a double detect pattern during the temporal moving situation.

In addition, as shown in Fig. 5, the detection process can be considered into four parts: region I (unexcited area), region II (backward heat conduction area), region III (exciting area), and region IV (excited area). In particular, the excited area can be further divided into the forward heat conduction area, the residual heat area, and the cooled area. Moreover, the forward heat conduction area and the exciting area constitute a heat superimposed area. The region of interest (ROI) is in exciting area and it will scan along the moving direction.

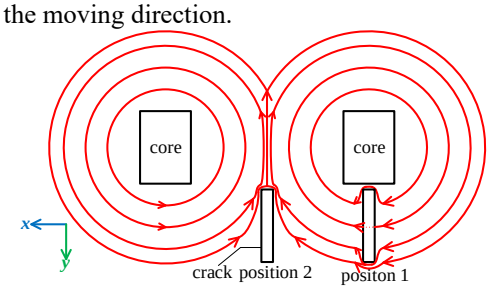

Fig. 4 Eddy currents paths when the crack at different positon.

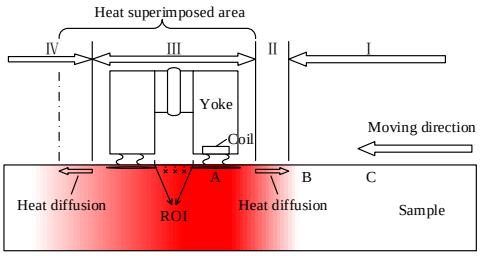

Fig. 5 Thermal imaging detection mechanism of the moving mode.

As shown in Fig. 5, the temperature in region I is the lowest (close to ambient temperature) because it is far away from the heating source and it cannot be affected by the heat conduction. The temperature in region II rises from right to left gradually due to the heat diffusion from the source. The temperature in region III rises dramatically because of the direct heating from the eddy current. In particular, the diminishing temperature in region IV is due to the increasing distance away from the yoke in spite of it has been heated before. According to the analysis above, it can be understood that the region which keeps the same distance from the yoke will probably present unequal temperature.

The scanning and exciting process can be illustrated in Fig. 6. In order of exciting, three points are selected as A, B, and C, respectively. At the time t_1, point A is excited and its temperature has increased rapidly while there exist defects. Meanwhile, the detection coil above this point will monitor its impedance and the voltage fluctuates obviously. In this instant, the time derivative term of $\vec{A}$ at point A moving with the coordinate system can be described as [31]:

$$\frac{\partial\vec{A}^{t+\Delta t}}{\partial t} = \frac{\partial\vec{A}}{\partial t} + (\vec{v}\cdot\nabla)\vec{A} \tag{14}$$

where Δt denotes the time interval, $\vec{A}$ is the vector potential and $\vec{v}$ is the velocity of specimen. Similarly, the time derivative term of T can be described as:

$$\frac{\partial T^{t+\Delta t}}{\partial t} = \frac{\partial T}{\partial t} + (\vec{v}\cdot\nabla)T \tag{15}$$

With the movement of the specimen, point A gradually moves away from the detection coil and its voltage will be recovered while the heat is spread around. When the time comes to t_3, the effect of heating point A disappears completely. Similarly, points B and C are excited at t_2, t_4 and eliminated the impacts at t_4, t_5, respectively. It should be noted that when point A is excited at t_1, the initial heat is not zero due to the heat diffusion from previous area. In addition, although the points after t_4 will generate heat and transfer to previous area, it cannot be recorded by IR camera because the ROI has already

changed and this part of heat should be ignored. If only the changes in heat from t_3 to t_4 are concerned, and completing all points from between t_1 and t_4, the total heat Q_{totalt} during this time can be given by:

$$Q_{totalt} = Q_{1t} + Q_{2t} + \cdots + Q_{nt} \quad (16)$$

where Q_{1t}, Q_{2t}, $\cdots$, Q_{nt} indicate the heat generated by all points between t_1 and t_4 from t_3 to t_4.

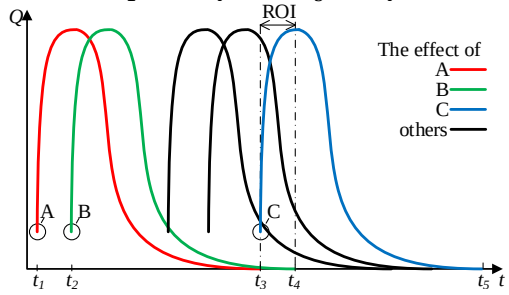

Fig. 6 Schematic diagram of the scanning and heating process.

In this detection, since the excitation yoke and thermal camera place relatively stationary, as a large temperature contrast occurs in the region of interest, for example, the above t_3-t_4, it can be applied to distinguish the defects.

III. SIMULATION AND EXPERIMENT SET-UP

A. Numerical experiment and discussion

Several numerical simulations based on the COMSOL Multiphysics 5.4 platform are performed in order to investigate the electromagnetic-thermal mechanism of the proposed system. The dynamic parametric scanning module has been constructed for ET and induction heating simulation experiments.

The geometric diagrams of this simulation model are carried out as shown in Fig. 7. Furthermore, the (a) top view and (b) side view, as well as the (c) space diagram, are presented respectively.

In the finite element simulation model, the number of scales has been interpreted directly in Fig. 7(a) and Fig. 7 (b), respectively. The outer and inner diameters as well as the height of the detection coils are 6.5 mm, 4.5 mm, and 3 mm. The length, width and thickness of the sample are 140 mm, 60 mm, and 10 mm. The length of the four artificial slots is 8 mm, the width is 1 mm and the depth of the four slots *a*-*d* are 5.5 mm, 6 mm, 6.5 mm, and 7 mm, respectively. In order to reduce the memory usage of the desktop, eddy current testing and induction heating simulations are implemented separately. Commonality, materials and their physical parameters (as listed in Table I) are critical to the simulations where the coils are composed of copper, the yoke is composed of alloy powder core ferrite and the samples are composed of the isotropic 45# steel (ferromagnetic material) or 316# stainless steel (non-ferromagnetic material) respectively. In the simulations of eddy current testing, the main parameters include conductivity, relative permittivity, and relative permeability. In the simulations of induction heating, the parameters of heat capacity, thermal conductivity, and density of these materials are also required. In addition, the excitation mechanism is same configuration that the selected lift-off distances in all simulation experiments are 2 mm, the turns of the coil probes are 570, the ambient temperature is 20 °C, the peak value of the excitation current is 100 A and its frequency is 180 kHz.

Table I The physical parameters of materials.

Parameters	copper	ferrite	45#	316#
conductivity (S/m)	5.99e7	1e-12	5.5e6	1.3e6
relative permittivity	1	1	1	1
relative permeability	1	5000	190	1
heat capacity (J/(kg·K))	385	600	475	502
thermal conductivity (W/(m·K))	400	5	51.9	12.1
density (kg/m^3)	8960	7800	7850	7990

a) Numerical simulations of eddy current testing

In the eddy current testing simulations, the method of parametric scanning is executed. As shown in Fig. 7 (c), the moving direction of the sample is the positive direction along the *x*-axis and the step is set to 2 mm. The simulated data is organized into Fig. 8. When the coils are marked as coil1-coil4 from the left side to the right side in Fig. 7 (c), it can be noticed that the data of coil1 is insignificant because the vertical cracks (parallel to the induced eddy current) never pass the directly below of it.

The purpose of the placement of coil1 is to detect horizontal defects that are insensitive to coil2-coil4. As the first coil approaches the sample, the voltage of coil4 drops sharply between the position of -55 mm and -40 mm because of the edge effect. It then stabilizes until the appearance of slot *a*. It is precisely seen that the voltage fluctuates during this time. Similarly, slot *b*, slot *c*, and slot *d* can be detected seriatim. There is a phase difference among voltage signals of coil4, coil3 and coil2 due to the time difference of the proximity of the defects. In particular, if crack becomes a horizontal one that can pass the below of coil1 during the movement, the situation will be changed that coil1 is sensitive. Fig. 8 (a) shows the tendency of voltage curves when the 45# steel is chosen to be the material of the sample, and the result is shown in Fig. 8 (b) when the material changed to be 316# stainless steel. Fig. 8 (c) shows the voltage curve of coil1 when the crack is horizontal. From this figure, the marked three points *a*, *b*, and *c* represent that the crack has just moved into the coil, the crack is exactly under the coil, and the crack has just moved out of the coil. The length of the

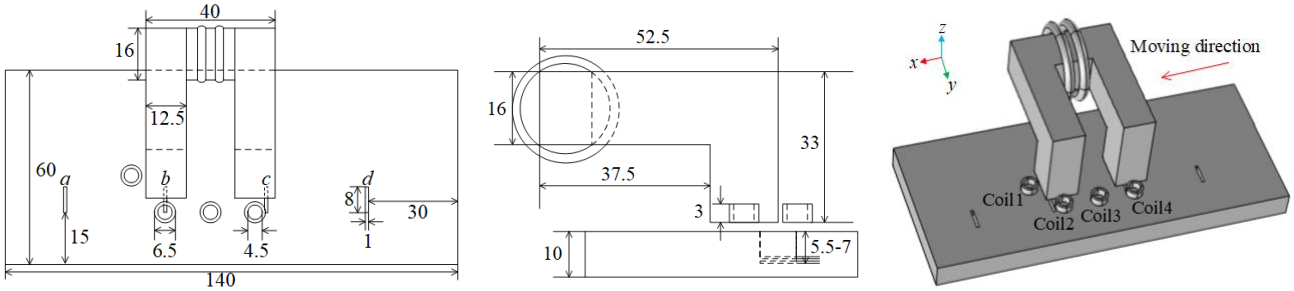

(a) Top view (b) Side view (c) Space diagram with the directions of *x*, *y*, *z*

Fig. 7 The geometric diagrams of the simulation model.

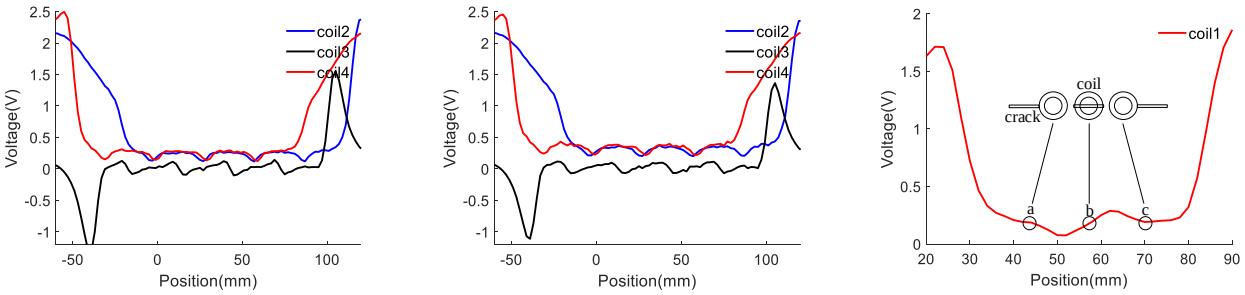

(a) 45# steel (b) 316# stainless steel (c) Horizontal defect

Fig. 8 The simulation voltage curves of coils.

crack can be expressed as:

$$l = s - d \tag{17}$$

where l denotes the length of the crack, s denotes the total distance of the crack moved, d denotes the outer diameter of the detection coil. It is worth noting that this formula can be only applied to horizontal cracks passing directly below the coil, otherwise, the angle should be included in the calculation. When the total distance s is replaced by the speed and time, Eq. (17) can be rewritten as:

$$l = vt - d \tag{18}$$

where v is the velocity of the sample and t is the time spent. Thus, if the velocity, time and outer diameter are given, the length of the crack can be estimated. It should be noted that the result can be inaccurate due to the error caused by a complex measurement environment, thus, it is necessary to take multiple measurements at different speeds and get the average value.

b) Numerical simulations of induction heating

The density of the induced eddy current and magnetic flux on the near-surface of the plate are shown in Fig. 9. In particular, the red arrows represent the current flow, the blue arrows represent the magnetic flux, and the size of the arrows is proportional to the intensity of the flow. It can be seen that the current flow and magnetic flux are perpendicular to each other. When a vertical crack moves below the ferromagnetic core, the induced current will flow around the crack, the density of the current on two sides of the defect grows higher than those of other areas. In ferromagnetic materials, the density of magnetic flux in plate is increased around the crack and this phenomenon is alleviated when in non-ferromagnetic materials. It will directly cause the heat generated by the hysteresis loss to be reduced drastically. This is the main reason that the L-shape yoke is sensitive to horizontal defects rather than vertical defects in non-ferromagnetic materials. Consequently, the supplement of ET is indispensable.

The distributions of temperature on the surface of the plate at 50 mm/s are presented in Fig. 10. When the plate was heated by the core, the heat will be gathered at the tip of the crack at the beginning (as shown in Fig. 10 (a)). Over time, heat will spread around. The edge of the crack will block the conduction of heat while it generates trailing smear based on the speed effect (as shown in Fig. 10 (b)).

B. Experimental study and validation

Experiments are executed to verify the feasibility of the system. The developed experimental system is shown in Fig. 11. It consists of a self-designed digital excitation source based on FPGA, an FLIR A655sc infrared camera with the temperature resolution of 0.08 K and the maximum recording frame rate of 200 Hz, a conveyor belt with the carrying speed of 50-250 mm/s, an NI USB-6366 DAQ card with the maximum sampling rate of 2 MHz and a laptop which is used for storing data.

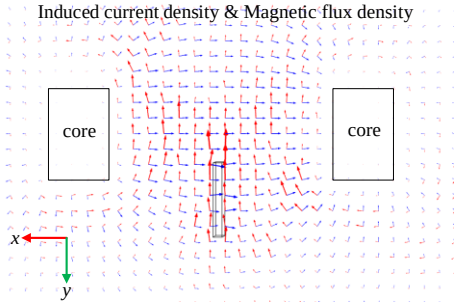

Fig. 9 Density of induced current and magnetic flux in simulation.

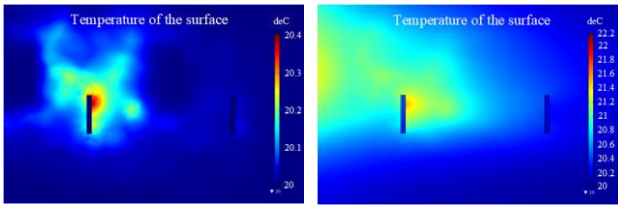

(a) At 0.05s (b) At 1s

Fig. 10 Distribution of temperature on the surface of the plate.

a) Design of the excitation source

Specifically, the digital excitation source is composed of a full-bridge LC resonant circuit, an FPGA control board, a high-power DC power supply, and an auxiliary power supply. The topology of the full-bridge LC resonant circuit is shown in Fig. 12. S_1-S_4 are four IPD110N12N3 power MOSFETs, V_s is the voltage provided by DC power supply and its value is set to 10 V for the test samples of 45# steel and 316# stainless (artificial cracks). And it is set to 40 V in the test sample of stainless steel (natural crack).

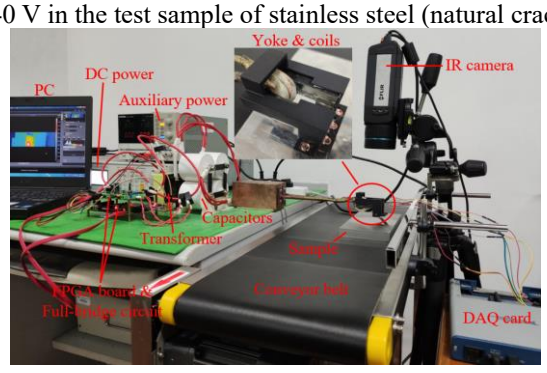

Fig. 11 Experimental system.

In addition, R_{eq} denotes the equivalent resistance of the circuit, it is typically ranged from several dozen to several hundred mΩ. C_r denotes the resonant capacitor and the value is 4.8 μF. L_r denotes the resonant

inductance and the value is 1 μH. The turns ratio of the transformer is 5:1. When the circuit works at the resonant state, the current flowing through the excitation coil reaches a peak value, and the magnetic field generated by the coil is the strongest. The resonant frequency of the series resonant circuit f_r can be described as:

$$f_r = \frac{1}{2\pi\sqrt{L_r C_r}} \tag{19}$$

The working logic of the excitation system can be summarized as follows: Firstly, the FPGA is programmed as the drive frequency sweep from 300 kHz-50 kHz and acquire the secondary current of the transformer during this process. Secondly, if this current value is greater than a set threshold, it means that the frequency is close to the resonant frequency and mark this value. Finally, the FPGA will stop sweeping and output at the marked frequency. Thus, the system will find the resonant frequency automatically and generate the maximum output power which is important to inspection.

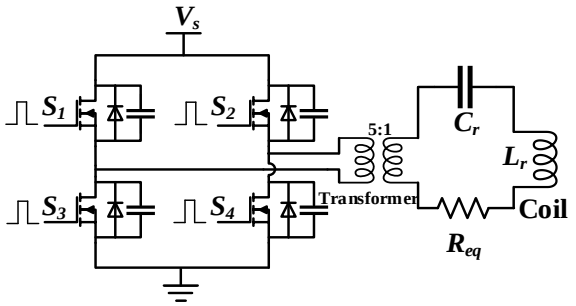

Fig. 12 Topology of the full-bridge LC resonant circuit.

b) Experimental validation

The isotropic samples are presented in Fig. 13 (a), from the left to right, they are 45# steel piece with four artificial cracks, 316# stainless steel piece with four cracks of the same specification, as well as the stainless steel piece from nuclear industry with a subsurface natural stress corrosion crack that cannot be directly observed. The dimensions of the 45# and 316# samples with four slots are consistent with the simulations (as shown in Fig. 7). And the length, width, thickness of the stainless steel piece are 200 mm, 100 mm, and 20 mm, respectively. However, the accurate length of the natrual crack is uncertain. As a comparison, the result of magnetic particle testing is presented in Fig. 13 (b) and from this picture, it can be inferred that the length of the crack is 50-60 mm.

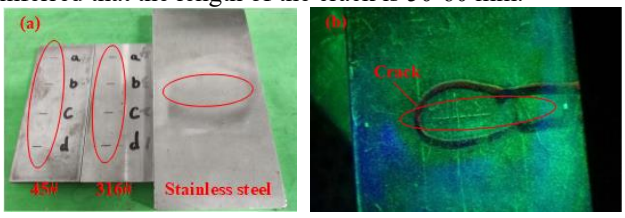

Fig. 13 (a) Isotropic samples. (b) Result of magnetic particle testing in stainless steel.

The samples are carried by the conveyor belt. The main settings of the experiments are illustrated as:

(1) The speeds of conveyor belt are selected to be 50 mm/s, 100 mm/s, 150 mm/s, 200 mm/s, and 250 mm/s, respectively. (2) The lift-off between the yoke and sample is 2 mm. (3) The valid values of excitation currents are 20A in the sample of 45# steel, 25A in the sample of 316# stainless and 100A in the sample of stainless steel piece. The excitation frequency is 181 kHz. (4) The sampling rate of the DAQ card is set to 1 MHz and the frame rate of the IR camera is 200 Hz and its resolution is 640×120 array.

Comparison experiments using a line-coil with wire diameter of 6 mm and a spiral-coil with the same wire diameter are configured. In particular, the radius of the spiral-coil is 22 mm and its turns are 3. To clarify, all of the experimental conditions are consistent except for the shape of the excitation coils.

c) Results analysis

After configuration, experiments can be carried out and the results are illustrated as follow:

1) Detection results of artificial cracks

In eddy current testing, in order to quantitative evaluate the detection sensitivity of the system, a parameter S is carried out which can be expressed as [32]:

$$S = \frac{\left|Max(v_{defect} - v_{normal})\right|}{Max(v_{nolmal})} \tag{20}$$

where S is the sensitivity of detection in the corresponding place, v_{defect} indicates the voltage value of coil probes when there is a defect and v_{normal} means no defect.

In this study, the reason for placing multiple detection coils is to improve the detectability since the variation of velocity has a limited impact on the values of S in the same material. Thus, to simplify the results, only the detection results of coil probes at the speed of 50 mm/s in 45# steel and 316# stainless are summarized in Fig. 15 and Fig. 16, respectively. The S values of detection results of different materials at the speed of 50 mm/s are displayed in Table II. It can be known from Fig. 15 and Fig. 16, there are voltages fluctuations at the occurrence of the defects, and the voltage variation of coil2 and coil4 is more pronounced than coil3. This is mainly because the magnetic flux near the end of the yoke poles is dense in the *z*-direction. The relative position of each defect and the interval between every two defects can be estimated based on times and speeds. The variation tendency of S is incremental from slot *a* to *d*, it is mainly because the depth of them are different and the coil probe is more sensitive to deeper cracks. Nevertheless, due to the complex test environment, it can only be used to roughly estimate the change in depth of the defects to some extent.

In thermal detection, the thermal contrast is generally used to quantify the sensitivity. The formula can be drawn as follow:

$$\mathrm{TC} = \frac{T_d - T_n}{T_n - T_0} \tag{21}$$

where TC is the thermal contrast, T_d is the temperature in defective area, T_n denotes the temperature in nondefective area and T_0 represents the ambient temperature.

The thermal images of slot *a-d* at the speed of 50 mm/s in 45# steel and 316# stainless are shown in Fig. 15 and Fig. 16, respectively. In comparison, the 4th row of them shows the testing results by adopting line-coil and the 5th row shows the testing results by adopting spiral-coil. In addition, some representative results at other speed are shown in Fig. 17. In this study, the cracks can be easily distinguished at each speed in 45# steel. However, it becomes more blurred as the speed increases in 316# stainless steel. It shows that the speed effect is unfavorable for ECT and the compensation of ET is necessary. It should be indicated that all of the thermal results use fixed subtraction except for 2nd row which uses the sliding subtraction processing (also

known as temporal differencing), which is a commonly used video processing method in moving mode. The process of this algorithm can be described as [33]:

$$D_n(x,y) = |f_n(x,y) - f_{n-1}(x,y)|, n = 2, \ldots, N \quad (22)$$

where $f_n(x,y)$ represents the temperature value of each pixel of the n^{th} frame, $D_n(x,y)$ is the pixel wise difference function and N is the number of thermal images. As shown in Fig. 14, it actually subtracts the previous frame from the next frame to obtain a new sequence while this captures the transient changes in temperature.

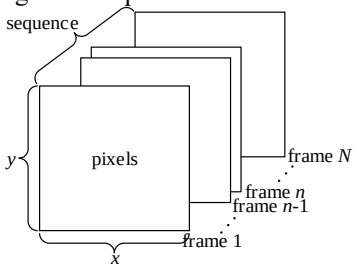

Fig. 14 Diagram of the thermal sequence.

An extra ruler guide is added to these images in order to judge the size of crack. As can be seen, in each coil, heat will be collected on both sides of the crack and generate trailing smear due to the speed effect, the results in the proposed configuration are better than the other two excitation structures under the same conditions. In addition, the detection results in ferromagnetic materials are better than those in non-ferromagnetic materials due to the heat generated by hysteresis loss. Particularly, it is significant difficult to detect the crack in 316# stainless when using the line-coil and spiral-coil. The TC values of the experimental results of different materials at the speed of 50 mm/s are displayed in Table II. The "–" refers no value. From these values, it can be indicated that the combination of the two sensing methods can strengthen the detectability and reliability. Furthermore, the surface emissivity and impurities of the samples will interfere with the evaluation of ECT. This is validated in Fig. 18 by painting the surface of the 45# steel with black strip near slot *b* and it can be noticed that ECT cannot distinguish the crack and strip in the thermal images due to the similarity characteristic for both defects and variation of emissivity. Thus, this detection challenge can be conquered with the supplement of ET as it enables the integrated system to distinguish the interference of the paint. Fig. 18 (d) shows the crack and black strip are well distinguished by detecting whether the coil voltage in this area fluctuates. In this way, the proposed system can not only retains the high resolution of ECT, but also avoids the interference of the impurities.

2) Detection results of natural stress corrosion cracks

In eddy current testing, the detection results of coil probes at the speed of 50 mm/s in stainless steel are summarized in Fig. 19. In particular, Fig. 19 (a) shows the detection direction of the crack is vertical (parallel to the eddy current flows), Fig. 19 (b) shows the detection direction of the crack is horizontal (perpendicular to the eddy current flows). Under these circumstances, coil1 plays an important role due to its complement to horizontal cracks detection. As shown in Fig. 19 (a), although the vertical crack can be detected by all coil probes, they are difficult to be shaped in ECT since natural defects of this angle in non-ferromagnetic materials are difficult to be heated. The horizontal cracks directly below the yoke can be imaged by ECT while they cannot be detected by coil2-coil4. Thus, the placement of coil1 can not only detects the horizontal cracks but also estimates their length under proper conditions. According to Fig. 19 (b), substituting the parameters into Eq. (18) of each speed and average repeatedly, the length of the natural stress corrosion crack can be calculated which it is ranged between 55 mm and 60 mm. The S value of detection result in stainless steel is added in Table II.

In thermal detection, the horizontal natural crack is observable when the speed is 50 mm/s, however it becomes blurred at 100 mm/s and the situation worsens with the increase of speed. Fig. 19 (b) shows the detection results of the thermal images at the speed of 50 mm/s in stainless steel. In comparison, Fig. 19 (c) shows the testing result by adopting line-coil and Fig. 19 (d) shows the testing result by adopting spiral-coil. It can be observed that the detection results of both using line-coil and spiral-coil are dissatisfactory under the speed effect, the crack can hardly be discovered by using line-coil and it is unclear by using spiral-coil. The TC values of different excitation coils in stainless steel are added in Table II, and the "×" refers to the crack cannot be detected in this way. From the results, compared with the line-coil and spiral-coil, the thermal contrast of the proposed mechanism is average enhanced with 55% and 64% in 45# steel, 68.3% and 62% in 316# stainless, as well as 120% and 70% in stainless steel. In addition, the supplement of the coil probes improves the detection sensitivity of the proposed structure average by 15.7%, 25.2% and 38.4% in the samples of 45# steel, 316# stainless, and stainless steel, respectively. These demonstrate the obvious superiority of the proposed detection system.

According to the change trend of the voltage curves and the temperature distribution of the thermal images, the above experimental results are consistent with the simulation results. In particular, the comparisons with the other two common excitation coils indicate that the proposed multiphysics structured system has strong detection capability and reliability.

IV. CONCLUSION AND FUTURE WORK

An efficient moving detection mode of a multiphysics structured system has been proposed. The theoretical analysis of dynamic eddy current testing and eddy current thermography has been presented. Both numerical simulations and verification experiments have been conducted to demonstrate the feasibility and detectability of the proposed system. Several conclusions can be drawn as follows: i) In the proposed model, the advantages of ET and ECT complemented each other, the coupling structure enhances the detectability and reduce the false alarm by reinforcing the evaluation of the defect region from two physics mechanisms simultaneously. ii) The required excitation current for the mechanism is small in metal plates inspection (45# steel 20 A, 316# stainless 25 A, natural micro-crack in stainless steel 100 A) due to the multiphysics structured model compared to conventional ECT. iii) The specimens can be evaluated fast by scanning at the speed of 50-250 mm/s which improved the speed of detection. iv) The results of the experiments verify the executability of the system and provide a method for estimating the length of horizontal cracks under specified conditions.

Future work will concentrate on multi-dimensional scanning detection of infrastructures which would probably by means of a robotic arm.

Table II The *S* and TC values of crack detection experiments.

		proposed				line-coil				spiral-coil			
slot		*a*	*b*	*c*	*d*	*a*	*b*	*c*	*d*	*a*	*b*	*c*	*d*
45#	TC(%)	157	185	185	185	120	118	129	125	114	114	114	114
	S(%)	13	14.3	17.7	17.9			–				–	
316#	TC(%)	114	114	114	114	33	50	50	50	66	66	66	50
	S(%)	17.5	21.7	23.7	38			–				–	
Stainless steel	TC(%)	120						×		50			
	S(%)	38.4						–		–			

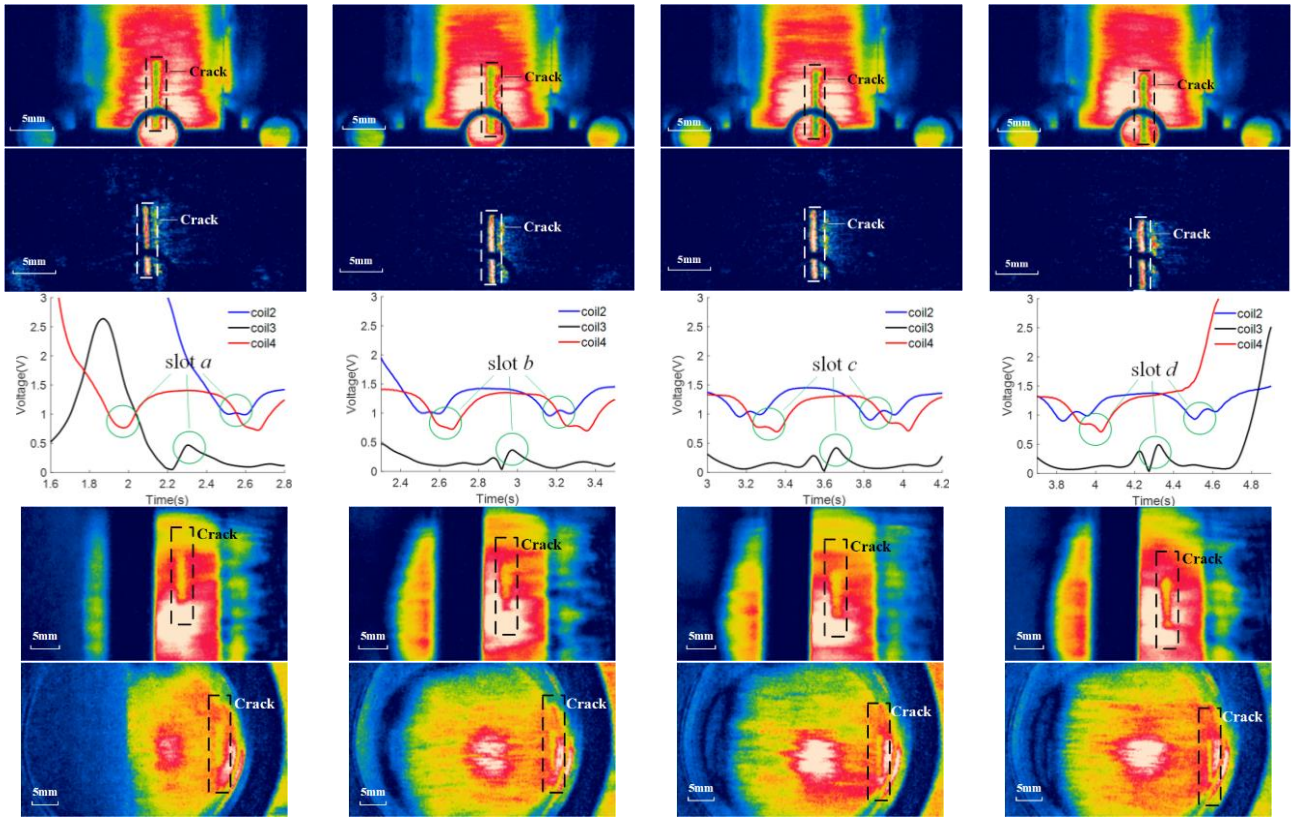

(a) slot *a* (b) slot *b* (c) slot *c* (d) slot *d*

Fig. 15 Experimental results of slot *a*-*d* in 45# steel by using the proposed structure (1st three rows), line-coil (4th row), spiral-coil (5th row) at the speed of 50 mm/s.

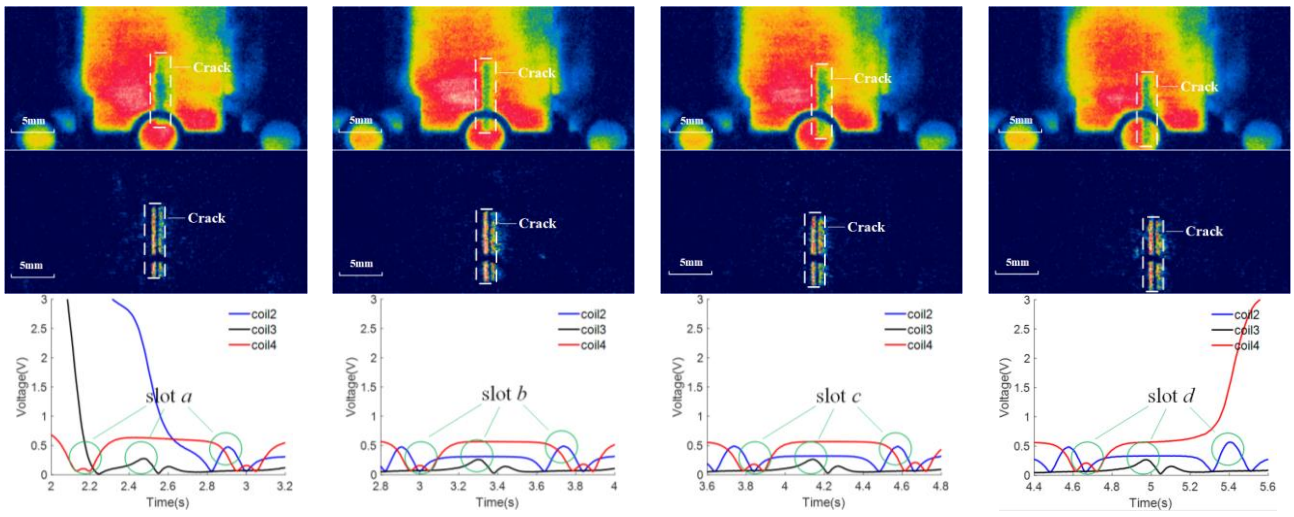

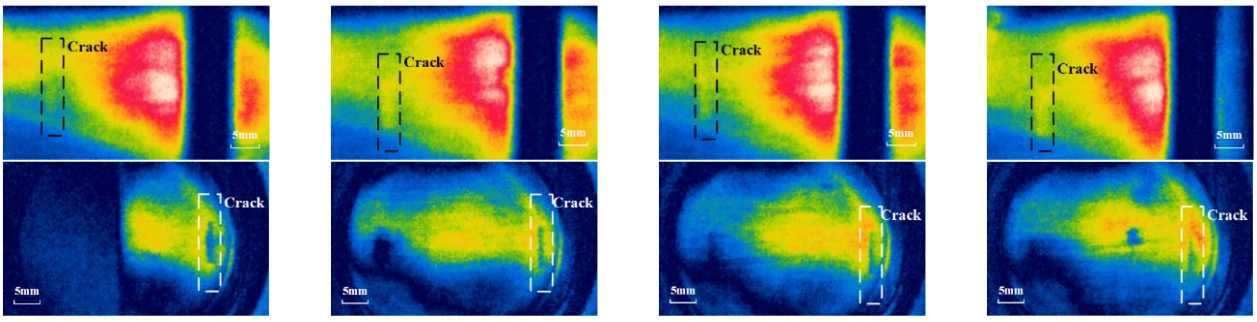

(a) slot *a* (b) slot *b* (c) slot *c* (d) slot *d*

Fig. 16 Experimental results of slot *a-d* in 316# stainless by using the proposed structure (1st three rows), line-coil (4th row), spiral-coil (5th row) at the speed of 50 mm/s.

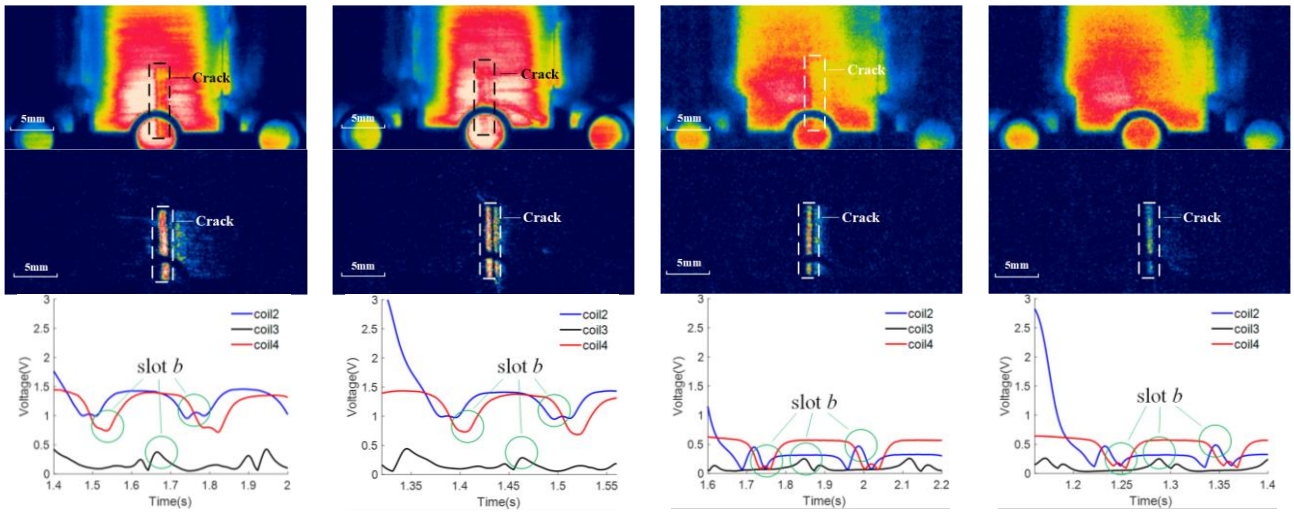

(a) slot *b*, 100mm/s, 45# steel (b) slot *b*, 250mm/s, 45# steel (c) slot *b*, 100mm/s, 316# stainless (d) slot *b*, 250mm/s, 316# stainless

Fig. 17 Experimental results of slot *b* in 45# steel and 316# stainless by using the proposed structure at the speed of 100 mm/s and 250mm/s.

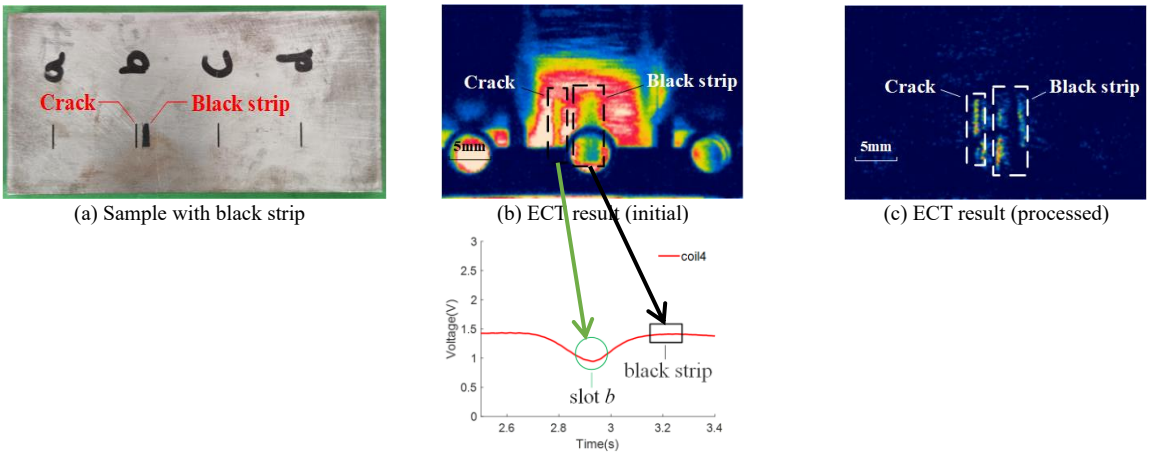

(a) Sample with black strip (b) ECT result (initial) (c) ECT result (processed)

(d) ET result

Fig. 18 Experimental results of integrated system to distinguish the interference of the black strip at the speed of 50 mm/s.

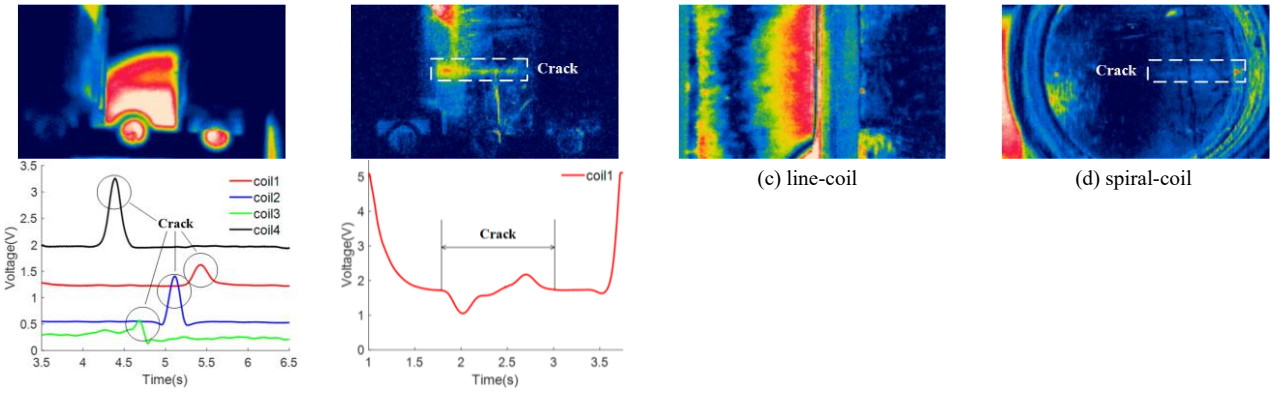

(a) vertical direction (b) horizontal direction (c) line-coil (d) spiral-coil

Fig. 19 Experimental results of the stainless steel plate by using (a)(b) the proposed structure, (c) line-coil, (d) spiral-coil the speed of 50 mm/s.

REFERENCE

[1] Trimm M. An overview of nondestructive evaluation methods[J]. Practical Failure Analysis, 2003, 3(3):17-31.

[2] Gao B , He Y , Woo W L , et al. Multidimensional Tensor-Based Inductive Thermography With Multiple Physical Fields for Offshore Wind Turbine Gear Inspection[J]. IEEE Transactions on Industrial Electronics, 2016, 63(10):6305-6315.

[3] Tian G Y, Yin A, Gao B, et al. Eddy Current Pulsed Thermography for Fatigue Evaluation of Gear[C]// American Institute of Physics, 2014.

[4] Yang R, He Y. Optically and Non-optically Excited Thermography for Composites: A Review[J]. Infrared Physics & Technology, 2016:S1350449515300542.

[5] Gao B, Woo W L, He Y, et al. Unsupervised Sparse Pattern Diagnostic of Defects With Inductive Thermography Imaging System[J]. IEEE Transactions on Industrial Informatics, 2015, 12(1).

[6] Lucia O, Maussion P, Dede E J, et al. Induction Heating Technology and Its Applications: Past Developments, Current Technology, and Future Challenges[J]. IEEE Transactions on Industrial Electronics, 2014, 61(5):2509-2520.

[7] Kasai N, Takada A, Fukuoka K, et al. Quantitative investigation of a standard test shim for magnetic particle testing[J]. NDT&E International, 2011, 44(5):421-426.

[8] Xue H, Yang Q. Nondestructive testing of pressure vessels: penetrant testing [J]. Nondestructive Testing, 2004.

[9] Bettayeb F, Haciane S, Aoudia S. Improving the time resolution and signal noise ratio of ultrasonic testing of welds by the wavelet packet[J]. NDT&E International, 2005, 38(6):478-484.

[10] Ghate M, Bhope K. Development, optimization and validation of ultrasonic testing for NDE of ELM coils[J]. Fusion Engineering and Design, 2017, 121:218-226.

[11] Wang G, Liao T W. Automatic identification of different types of welding defects in radiographic images[J]. NDT&E International, 2002, 35(8):519-528.

[12] Morozov M, Rubinacci G, Tamburrino A, et al. Numerical models of volumetric insulating cracks in eddy-current testing with experimental validation[J]. IEEE Transactions on Magnetics, 2006, 42(5):1568-1576.

[13] Fan M, Huang P, Ye B, et al. Analytical modeling for transient probe response in pulsed eddy current testing[J]. NDT&E International, 2009, 42(5):376-383.

[14] Abidin I Z, Tian G Y, Wilson J, et al. Quantitative evaluation of angular defects by pulsed eddy current thermography[J]. NDT&E International, 2010, 43(7):537-546.

[15] Cheng L, Gao B, Tian G Y, et al. Impact Damage Detection and Identification Using Eddy Current Pulsed Thermography Through Integration of PCA and ICA[J]. IEEE Sensors Journal, 2014, 14(5):1655-1663.

[16] Zhang H, Sfarra S, Sarasini F, et al. Optical and Mechanical Excitation Thermography for Impact Response in Basalt-Carbon Hybrid Fiber-Reinforced Composite Laminates[J]. IEEE Transactions on Industrial Informatics, 2017, 99:1-1.

[17] Yang R, He Y, Gao B, et al. Lateral heat conduction based eddy current thermography for detection of parallel cracks and rail tread oblique cracks[J]. Measurement, 2015, 66:54-61.

[18] He Y, Tian G Y, Pan M, et al. An investigation into eddy current pulsed thermography for detection of corrosion blister[J]. Corrosion Science, 2014, 78:1-6.

[19] He Y, Yang R. Eddy Current Volume Heating Thermography and Phase Analysis for Imaging Characterization of Interface Delamination in CFRP[J]. IEEE Transactions on Industrial Informatics, 2015, 11(6):1287-1297.

[20] R. Yang, Y. He. Optically and non-optically excited thermography for composites: A review, Infrared Phys. Technol. 75 (2016) 26–50.

[21] Macecek M. Advanced eddy current array defect imaging[J]. NDT&E International, 1997, 30(3):178-178(1).

[22] Sun Z, Cai D, Zou C, et al. A Flexible Arrayed Eddy Current Sensor for Inspection of Hollow Axle Inner Surfaces[J]. Sensors, 2016, 16(7).

[23] Endo H, Koike M, Matsui T, et al. Natural Crack Sizing Based on Eddy Current Image and Electromagnetic Field Analyses[C]// Aip Conference. American Institute of Physics, 2006.

[24] He Min, Zhang Laibin, Zheng Wenpei, et al. Crack detection based on a moving mode of eddy current thermography method[J]. Measurement, 109:119-129.

[25] He M, Zhang L, Li J, et al. Methods for suppression of the effect of uneven surface emissivity of material in the moving mode of eddy current thermography[J]. Applied Thermal Engineering, 2017, 118(Complete):612-620.

[26] Gao Y, Tian G Y, Li K, et al. Multiple cracks detection and visualization using magnetic flux leakage and eddy current pulsed thermography[J]. Sensors & Actuators A Physical, 2015.

[27] Li K, Tian G Y, Cheng L, et al. State Detection of Bond Wires in IGBT Modules Using Eddy Current Pulsed Thermography[J]. IEEE Transactions on Power Electronics, 2014, 29(9):5000-5009.

[28] Liu Z, Gao B, Tian G Y. Natural Cracks Diagnosis System based on Novel L-shaped Electromagnetic Sensing Thermography[J]. IEEE Transactions on Industrial Electronics, 2019, PP(99):1-1.

[29] Goldammer M, Mooshofer H, Rothenfusser M, et al. Automated Induction Thermography of Generator Components[J]. AIP Conference Proceedings, 2010, 1211:451-457.

[30] Streza M, Longuemart S, Guilmeau E, et al. An active thermography approach for thermal and electrical characterization of thermoelectric materials[J]. Journal of Physics D: Applied Physics, 2016, 49(28):285601.

[31] Shin Y K, Sun Y. Numerical techniques for solving magnetostatic problems involving motion and nonuniform geometry[J]. IEEE Transactions on Magnetics, 1997, 33(2):P.1161-1166.

[32] Yang C, Gao B, Ma Q, et al. Multi-Layer Magnetic Focusing Sensor Structure for Pulsed Remote Field Eddy Current[J]. IEEE Sensors Journal, 2018:1-1.

[33] A. J. Lipton, H. Fujiyoshi and R. S. Patil. Moving target classification and tracking from real-time video, Proceedings Fourth IEEE Workshop on Applications of Computer Vision. WACV'98 (Cat. No.98EX201), Princeton, NJ, USA, 1998, pp. 8-14.